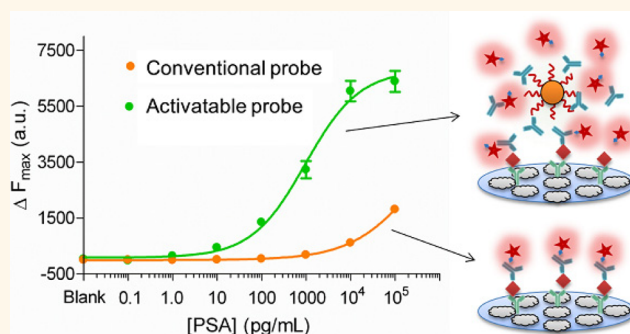# Gold Nanoparticle-Based Activatable Probe for Sensing Ultralow Levels of Prostate-Specific Antigen

Dingbin Liu,[†] Xinglu Huang,[†] Zhantong Wang,[‡] Albert Jin,[§] Xiaolian Sun,[†] Lei Zhu,[†,‡] Fu Wang,[†] Ying Ma,[†] Gang Niu,[†] Angela R. Hight Walker,[⊥] and Xiaoyuan Chen[‡,*]

[†]Laboratory of Molecular Imaging and Nanomedicine, National Institute of Biomedical Imaging and Bioengineering, National Institutes of Health, Bethesda, Maryland 20892, United States, [‡]Center for Molecular Imaging and Translational Medicine, School of Public Health, Xiamen University, Xiamen 361005, China, [§]Laboratory of Cellular Imaging and Macromolecular Biophysics, National Institute of Biomedical Imaging and Bioengineering, National Institutes of Health, Bethesda, Maryland 20982, United States, and [⊥]Optical Technology Division, Physics Laboratory, National Institute of Standards and Technology, Gaithersburg, Maryland 20899, United States

ABSTRACT It is still in high demand to develop extremely sensitive and accurate clinical tools for biomarkers of interest for early diagnosis and monitoring of diseases. In this report, we present a highly sensitive and compatible gold nanoparticle (AuNP)-based fluorescence-activatable probe for sensing ultralow levels of prostate-specific antigen (PSA) in patient serum samples. The limit of detection of the newly developed probe for PSA was pushed down to 0.032 pg/mL, which is more than 2 orders of magnitude lower than that of the conventional fluorescence probe. The ultrahigh sensitivity of this probe was attributed to the high loading efficiency

of the dyes on AuNP surfaces and high fluorescence quenching—unquenching abilities of the dye—AuNP pairs. The efficiency and robustness of this probe were investigated in patient serum samples, demonstrating the great potential of this probe in real-world applications.

KEYWORDS: fluorescence-activatable probe · gold nanoparticle · prostate-specific antigen (PSA) · rhodamine B isothiocyanate (RBITC)

W e report a fluorescence-based activatable immunoassay for ultrasensitive detection of cancer biomarkers in a panel of serum samples. A biomarker is defined as the "molecular signature" of a physiological or disease process at certain stages and is therefore particularly useful for diagnosing disease, monitoring disease progression, and evaluating therapeutic response.[1,2] Many diseases such as cancers are much more susceptible to treatment when diagnosed in the early stages, indicating that earlier diagnosis of the disease may enable improved therapeutic intervention.[3] However, the levels of biomarkers are often low in biological samples from patients.[4,5] It is therefore extremely important to develop ultrasensitive biosensors for biomarkers of interest.

The current gold standard for clinical biomarker detection is the enzyme-linked immunosorbent assay (ELISA). However, due to its moderate sensitivity, ELISA usually allows detection only after biomarker levels have already reached critical threshold concentrations, at which point the disease has already advanced remarkably. Thus, ultrasensitive assays are urgently required for detection of biomarkers in the clinic. Nanotechnology is already playing an increasingly important role in the design of ultrasensitive biosensors.[6–8] In the past few decades, many efforts have been made to create signal transducers such as fluorescence,[9–13] biobarcodes,[14,15] Raman dyes,[16] and enzymes[17,18] for signal amplification. Many of these approaches showed good sensitivity, but most of them relied on bulky and advanced instruments, thus making them difficult to be widely applied in the real world as point-of-care (POC) diagnostics. Generally applicable readouts such as fluorescence for
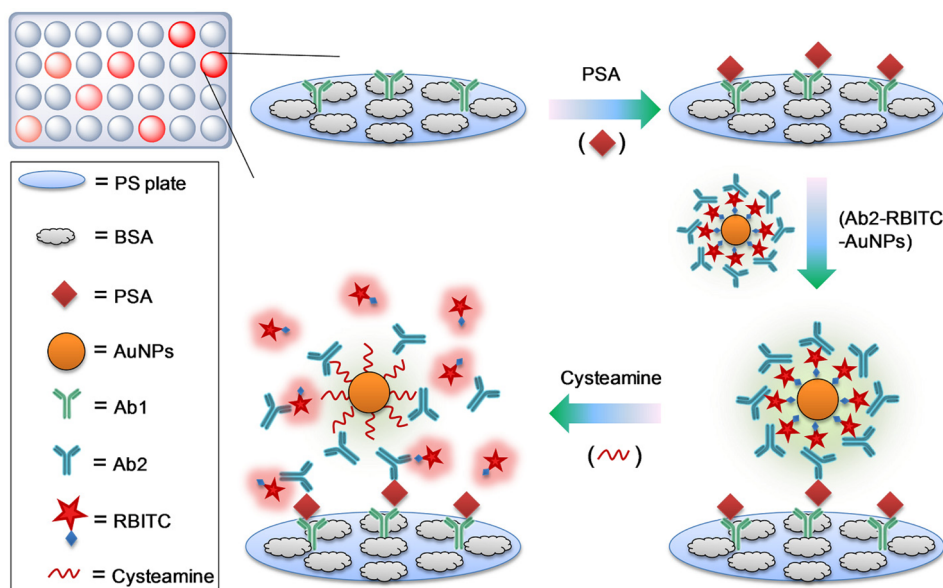
Scheme 1. Representation of the fluorescence-activatable immunoassay for PSA performed in 96-well PS plates.

immunoassays have the potential to revolutionize analytical sciences because of their good compatibility with the currently available analytical platforms in the clinic. However, the sensitivity of conventional fluorescence immunoassays is insufficient for monitoring biomarkers in most settings where the levels of biomarkers are extremely low. To improve the sensitivity for detecting low-abundance biomarker proteins, most reported fluorescence assays focused on creating new three-dimensional surfaces to increase the density of capture antibodies and the antibody orientation, thus enhancing the antibody—antigen binding efficiency for signal amplification.[19,20] The fabrication of new surfaces is inconvenient and costly, and thereby appears to be poorly suited for POC diagnostics.

Recently, fluorescence-activatable probes have been demonstrated as an effective optical imaging tool for targets of interest with superior contrast.[21] The very high surface area-to-volume ratio and quenching ability of gold nanoparticles (AuNPs) enable this type of platform to be promising in constructing ultrasensitive probes for biomarkers. Herein, we present a new activatable probe to augment the detection sensitivity of fluorescent ELISA assays for prostate-specific antigen (PSA) in serum samples. Rhodamine B isothiocyanate (RBITC) was employed as the model fluorescent dye, thousands of which were loaded onto each AuNP to form RBITC—AuNP conjugates. The RBITC layer of the nanoconjugates was covered with detection antibodies (Ab2) through electrostatic interactions, thus retaining their biological activity toward the target antigen. As depicted in Scheme 1, in the presence of targeted biomarker PSA, the Ab2—RBITC—AuNPs conjugates were pulled down onto the substrate. In this state, the fluorescence of RBITC was highly quenched by AuNPs. Upon addition of cysteamine into the

detection system, the attached RBITC molecules were competitively removed from AuNP surfaces, leading to the significant recovery of RBITC fluorescence. The intensity of the recovered fluorescence is well proportional to the concentration of the biomarkers in serum samples.

RESULTS AND DISCUSSION

A fluorescence-activatable probe is typically composed of two parts: a fluorescent dye that acts as the donor and a quencher that acts as the acceptor. In this report, we chose RBITC as the model fluorescent dye for three reasons: (1) RBITC contains an isothiocyanate (ITC) group, which is a high-affinity anchoring group commonly used to attach organic molecules onto colloidal nanoparticles. (2) RBITC is water-soluble and strongly fluorescent. In addition, the fluorescence of RBITC can be effectively quenched by AuNPs. In the presence of a high concentration of thiol-containing compounds, RBITC can be readily removed from AuNP surfaces, leading to the recovery of fluorescence. (3) RBITC contains two positively charged quaternary ammonium groups, which can bind with the negatively charged groups on Ab2 through electrostatic interactions. In addition, we chose AuNPs as the unique quencher for RBITC dyes owing to their extremely high quenching efficiencies (up to 99.8%).[21,22] When the two components are in close proximity, the fluorescence of RBITC is highly quenched *via* the nanoparticle surface energy transfer (NSET) effect.

As a proof of concept, we first prepared the activatable fluorescent probe that is composed of detection antibodies, RBITC molecules, and AuNPs. The commercially available AuNPs are commonly stabilized with a citrate coating, which can be readily replaced by thiol-containing compounds. In this study, we took 15 nm

AuNPs as an example to demonstate the procedure of preparing Ab2−RBITC−AuNPs (Figure S1A in the Supporting Information). We first prepared RBITC−AuNPs *via* a ligand exchange approach.[23] Briefly, to the original citrate-AuNPs solution (1 mL, 2.3 nM) was added 20 μL of K_2CO_3 solution (100 mM) to yield a pH 9.0 mixture, and then 1 μL of RBITC (10 mM) was added into the mixture under vigorous shaking. After 1 h of equilibration, the resulting solution was centrifuged to remove the excess amount of RBITC, and the pellet was redispersed in 1 mL of K_2CO_3 solution (pH 9.0). Later, Ab2 (10 μL, 1 mg/mL) was added into the RBITC−AuNPs solution, and the mixture was allowed to shake mildly at room temperature for 2 h. Finally, the remaining active sites of the RBITC layer were passivated with 1 mL of bovine serum albumin (BSA, 10% solution in 10 mM phosphate-buffered saline (PBS)) to prevent the nonspecific binding when conducting the immunoassay detection.

The functionalized AuNPs were characterized by dynamic light scattering (DLS) (Figure S1B in the Supporting Information). The average hydrodynamic diameter of RBITC−AuNPs is 29.4 ± 1.3 nm, which is similar to that of the citrate-AuNPs (30.5 ± 0.95 nm). It is worth noting that the thickness of the organic layer on AuNPs has not increased, demonstrating that the RBITC molecules were adsorbed onto AuNP surfaces by replacing citrate rather than attaching onto the negatively charged citrate layer *via* electrostatic interactions. After the Ab2 functionalization and BSA passivation, the average hydrodynamic diameter of nanoparticles increased significantly to 103.4 ± 6.7 nm. We employed zeta potential measurements to further explore the surface charge variations of AuNPs before and after modification (Figure S1C in the Supporting Information). As we expected, the zeta potential of RBITC−AuNPs was close to neutral (1.15 ± 2.35 mV). When Ab2 was added onto the RBITC layer, the charge of the nanoparticles became negative (−19.4 ± 1.3 mV), most likely owing to the acidic groups in Ab2 and BSA. To further confirm the quality of AuNPs after RBITC and Ab2 coating, the AuNPs were characterized using UV−vis spectroscopy. As shown in Figure S2 (in the Supporting Information), 15 nm AuNPs had a typical absorption band at around 520 nm, while the appearance of a new peak at around 555 nm was attributed to the RBITC absorbance of the RBITC−AuNP conjugates.

After obtaining the Ab2−RBITC−AuNPs-activatable probe, we demonstrated that RBITC can be effectively released from AuNP surfaces in the presence of a high concentration of thiol-containing compounds. We first compared the release abilities of different thiol-containing compounds. Among the thiol compounds (1 mM thiols for each compound) used in this study, we noted that smaller sized molecules showed higher efficiency to release RBITC from the AuNP surfaces.

It is reasonable that smaller compounds suffer from less stereohindrance to react with AuNP surfaces, making the displacement reaction easier. Cysteamine, the smallest compound used in this study, was found to be the best release reagent for the activatable probe (Figure S3 in the Supporting Information). After adding cysteamine (1 mM) into the Ab2−RBITC−AuNPs solution, the color of the solution changed from red to blue immediately (Figure 1A, top panel). This phenomenon was attributed to the formation of cysteamine−AuNP aggregates, further demonstrating the cysteamine-triggered displacement reaction. The color change was accompanied by a decrease of absorption band at 520 nm and the appearance of a new peak between 600 and 800 nm in the UV−vis spectra (Figure 1B). Simultaneously, the addition of cysteamine induced the removal of RBITC from AuNP surfaces, thus leading to the significant recovery of RBITC fluorescence (Figure 1A, bottom panel). As shown in Figure 1C, the fluorescence recovery is around 60% (blue line) of the initial state (red line). Additionally, we optimized the concentration of cysteamine applied in this system. With the increase of cysteamine, the RBITC fluorescence recovered gradually, and the maximal value was reached when the concentration of cysteamine was up to 1 mM (Figure 1D). The fluorescence recovery process was also time-dependent. After addition of cysteamine (1 mM), the RBITC fluorescence increased significantly in 1 min and then kept constant with time (Figure S4 in the Supporting Information). The results revealed that the displacement reaction can be completed quickly.

To evaluate the efficiency of this activatable nanosensor, the as-prepared Ab2−RBITC−AuNPs were brought into the sandwich ELISA for PSA, the United States Food and Drug Administration (FDA)-approved prostate cancer biomarker. Since the size of AuNPs plays a critical role in quenching fluorescence of dyes,[24] it is worth comparing the detection performance of the Ab2−RBITC−AuNPs tags with different sized AuNP cores. Based on the formula surface area of a sphere = $4\pi(D/2)^2$ (D = diameter), larger AuNPs have larger surface areas and are thus capable of loading more RBITC. To demonstrate that the detection performance is dependent on the quenching nature of particle size other than the amount of RBITC on a Au surface, we fixed the total surface area of 1 mL of AuNPs with diameters of 15, 30, 60, and 80 nm, where their concentrations were calculated to be 2.3, 0.58, 0.143, and 0.081 nM, respectively. By measuring the absorbance of RBITC before and after loading onto AuNPs, as we expected, the amount of RBITC loaded onto each sized AuNPs was approximately the same (Figure S5 in the Supporting Information). With the assistance of a standard curve (Figure S6 in the Supporting Information), the numbers of RBITC on each of 15, 30, 60, and 80 nm AuNPs were estimated to be 2800, 10 000, 40 500, and 71 600, respectively.
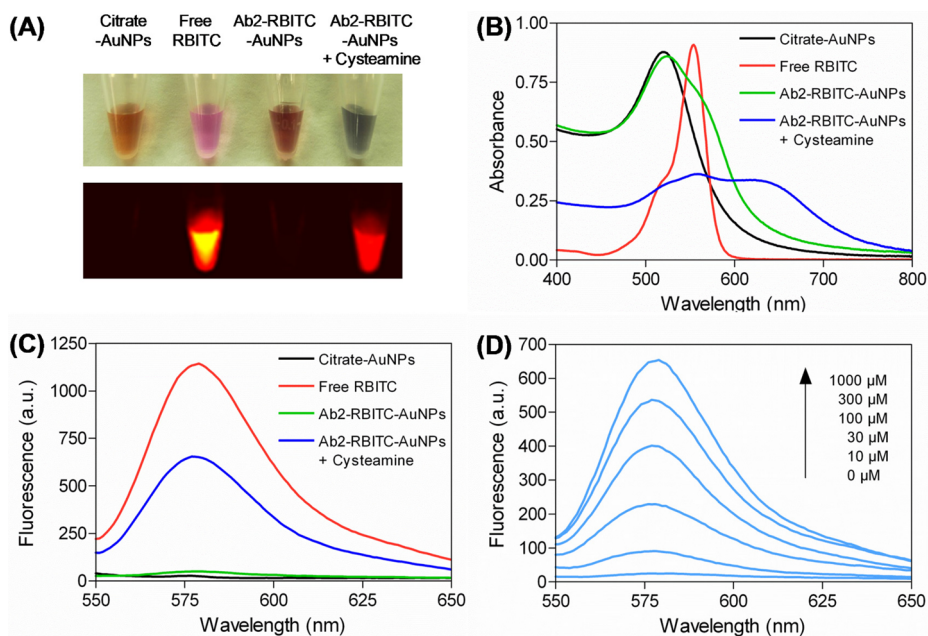
Figure 1. (A) Bright-field and fluorescence images of solutions containing citrate-AuNPs, free RBITC, Ab2−RBITC−AuNPs, and Ab2−RBITC−AuNPs treated with 1 mM cysteamine. Absorption spectra (B) and fluorescence emission spectra (C) of solutions containing citrate-AuNPs, free RBITC, Ab2−RBITC−AuNPs, and Ab2−RBITC−AuNPs treated with 1 mM cysteamine. (D) Fluorescence emission spectra of Ab2−RBITC−AuNPs solutions treated with various concentrations of cysteamine ranging from 0 to 1 mM. The spectra were collected 1 min after the addition of cysteamine.

We next compared the detection performance of sandwich ELISA by using Ab2−RBITC−AuNPs with diameters of 15, 30, 60, and 80 nm. For all the four sized Ab2−RBITC−AuNPs, the total amount of loaded RBITC remained the same. We performed the detection in the commonly used 96-well polystyrene (PS) plates. As the first step, we immobilized anti-PSA capture antibodies (Ab1) onto the PS substrate, followed by adding 1% BSA as blocking agent. Then, PSA-spiked PBS solutions containing 0.05% Tween 20 (PBST) were added at concentrations ranging from 0.1 to 10^5 pg/mL along with a PBST-only blank and incubated for 1 h at 37 °C. After rinsing with PBST, Ab2−RBITC−AuNPs solutions were added into the wells. Figure S7 (in the Supporting Information) clearly demonstrated that (1) higher concentrations of PSA can capture more Ab2−RBITC−AuNPs. Therefore, upon the addition of cysteamine (1 mM), more RBITC molecules can be released from AuNP surfaces, thus resulting in stronger fluorescence recovery. (2) Larger AuNPs induce stronger fluorescence recovery. This phenomenon is very attractive to guide the design of high-sensitivity nanosensors.

We further investigated the reason that larger sized AuNPs provided higher sensitivity. Since different sizes of AuNPs exhibit different extinction coefficients (Table S1 in the Supporting Information) and surface plasmon resonance (SPR) bands in the visible spectral regions, both of which directly affect their fluorescence quenching efficiencies,[25] we therefore compared the NEST effects of the four sized AuNPs toward RBITC. By successive addition of different concentrations of citrate-AuNPs into solutions containing a fixed

concentration (1 μM) of RBITC, we found that more citrate-AuNPs led to higher efficiency fluorescence quenching. On the basis of the plots of F_0/F values *versus* AuNP concentrations, the Stern−Volmer relationship between AuNP concentration and RBITC fluorescence intensity was obtained by the equation $F_0/F = 1 + K_{SV}[Q]$, where F_0 and F are the fluorescence intensity of RBITC in the absence and presence of AuNP quencher, respectively; K_{SV} is the Stern−Volmer quenching constant; and [Q] is the concentration of the AuNP quencher. From the results plotted in Figure 2, we noted that, for all four sized AuNPs, the relationship between concentrations of AuNP quencher and F_0/F values was linear only in the low concentrations of AuNP regions and showed an upward deviation from linearity upon further increasing the concentrations of AuNPs. This can be explained by the combined effects of static quenching and dynamic quenching. The K_{SV} values are derived from the slopes in Figure 2 to be 3.485×10^9, 2.307×10^{10}, 1.132×10^{11}, and 2.126×10^{11} M^{-1} for AuNPs with diameters of 15, 30, 60, and 80 nm, respectively. The K_{SV} values reveal that, with the increase of particle diameter, the quenching efficiency of AuNPs increases dramatically. In addition, the K_{SV} values of $10^9 - 10^{11}$ M^{-1} are several orders of magnitude higher than those of small organic dye−inorganic quencher pairs.[26] On the basis of the findings, we reasoned that larger AuNPs show higher quenching efficiency that generates lower background signal. Apart from this, larger AuNPs can load more RBITC, and thus more RBITC can be removed from AuNP surfaces. We therefore can conclude that lager AuNPs may offer better detection performance.
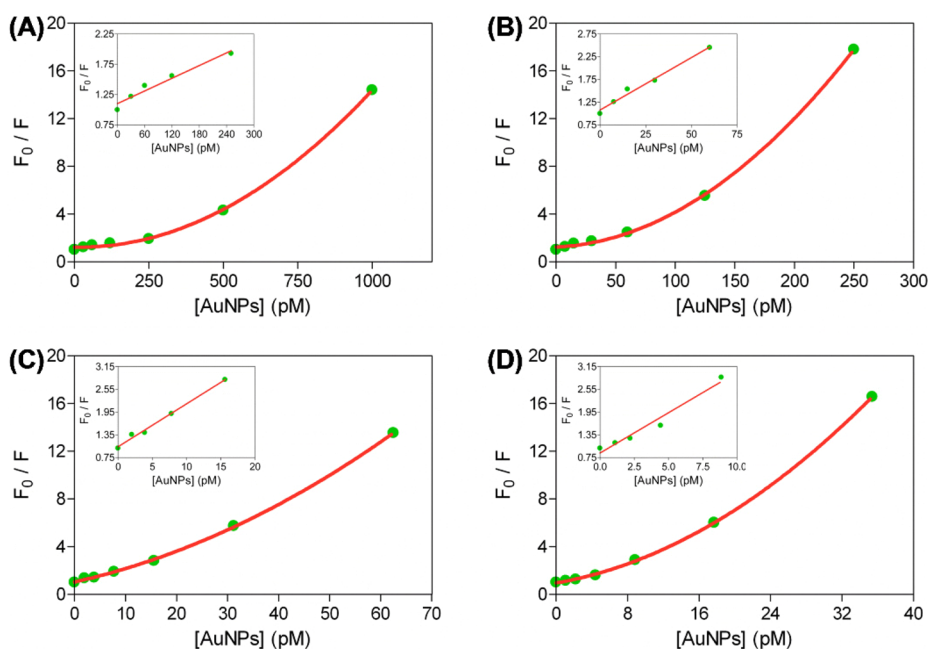
Figure 2. Stern−Volmer plots of RBITC quenching by varying concentrations of AuNPs with diameters of 15 (A), 30 (B), 60 (C), and 80 nm (D), respectively. F_0 and F represent fluorescence intensity of RBITC in the absence and presence of AuNP quencher, respectively.

To demonstrate that our fluorescence-activatable probe is superior to conventional fluorescence ELISA probes, we prepared fluorescent Ab2 by labeling anti-PSA Ab2 with RBITC. The ITC group in RBITC is a reactive group that is commonly used to conjugate with the primary amines of proteins without generating a leaving group. The conjugation reaction was performed in alkaline solution (pH 9.0), where the target amine groups in Ab2 are mainly unprotonated. Each Ab2 is usually allowed to conjugate with 3−5 RBITC dyes because higher conjugations can cause internal quenching between the dyes and influence the immunogenic activity of Ab2.[27] After the conjugation, the anti-PSA Ab2 showed a typical RBITC emission peak at around 580 nm, demonstrating that RBITC had been successfully labled onto Ab2 (Figure S8 in the Supporting Information). Later, we compared the detection performance of the RBITC-labeled Ab2 with our activatable Ab2−RBITC−AuNPs probes (30 nm AuNPs were applied as the core). Figure 3 depicted the ELISA signals for the two probes. As indicated clearly by the ΔF_{max} values ($\Delta F_{max} = F - F_0$, where F is the emission fluorescence intensity at 590 nm and F_0 is the background fluorescence), the activatable probe showed much higher ELISA signals than that of the conventional fluorescence probe. On the basis of a signal-to-noise ratio of 3, the limit of detection (LOD) of the activatable probe is determined to be 0.032 pg/mL, which exceeds the LOD of the conventional fluorescence probe (10.23 pg/mL) by more than 2 orders of magnitude. The sensitivity of the newly developed activatable probe is extremely attractive because the serum concentrations of biomarkers in most diseases

are at pg/mL levels, which is too low to be monitored by the current comercial immunoassays.[28]

The ability of the activatable probe to monitor much lower concentrations of biomarkers than conventional fluorescence ELISA is due to two effects: (1) high efficiency of dye loading and detaching from AuNP surfaces and (2) very low background signals when detected. The sensitivity of any immunoassay is determined by the antibody−antigen affinity, the label efficiency, and the background signals. Since the affinity of the antibody−antigen is given, the sensitivity of this probe is therefore determined by the loading and detaching efficiency of the dye and the background signals. AuNPs can carry thousands of RBITC *via* the formation of Au−S bonds,[29−32] and the majority of them can be released from AuNP surfaces in the presence of cysteamine, causing very strong fluorescence recovery. In addition, the remaining active sites of the RBITC layer on AuNPs were effectively passivated by BSA, indicating that the nanoconjugates became inert to other components involved in the detection system. As a result, the Ab2−RBITC−AuNPs probes induced negligible nonspecifc adsorption and thus led to very low background signals. The binding of Ab2−RBITC−AuNPs to the PSA-immobilized substrates was further confirmed by atomic force microscopy (AFM). The pretreated-PSA concentration was 1 ng/mL. As shown in Figure 4, a lot of Ab2−RBITC−AuNPs were immobilized onto the substrate *via* antibody−antigen interactions, while very few Ab2−RBITC−AuNPs are observed on the substrate treated by the PBST-only samples.

To further assess the effeciency and applicability of this highly sensitive activatable probe, we investigated
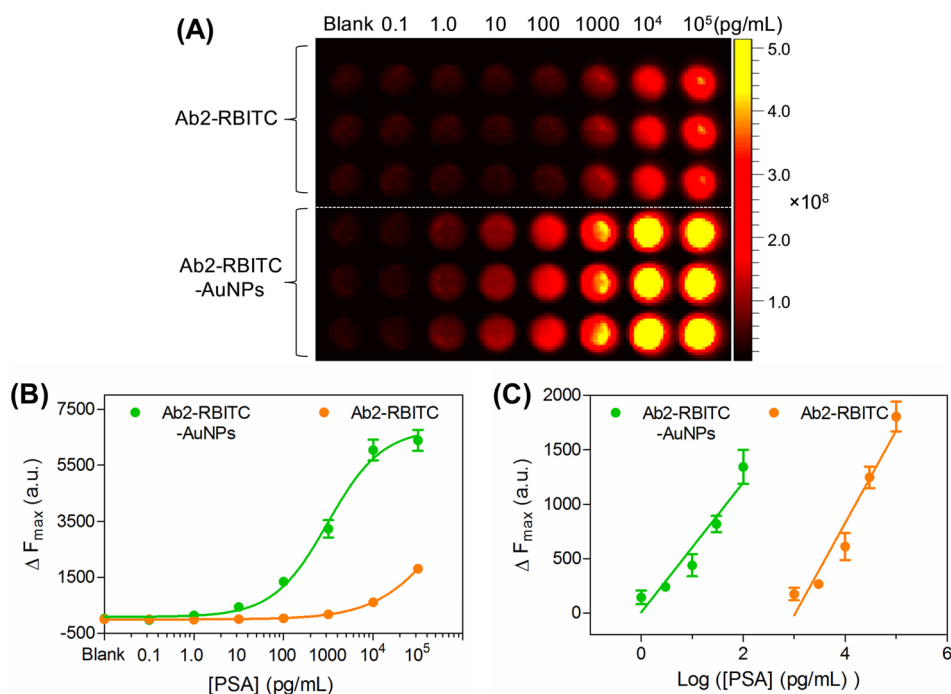
Figure 3. Conventional fluorescent immunoassay and the activatable immunoassay for sensing various concentrations of PSA in a 96-well PS plate. (A) Top panel: Fluorescence images of the commonly used fluorescent probe for various concentrations (0.1 pg/mL to 100 ng/mL) of PSA using Ab2—RBITC as detection tags. Bottom panel: Fluorescence images of the newly developed fluorescence-activatable probe for the same concentrations of PSA. (B) Comparison of the detection performance of the two probes by plotting fluorescence intensity at 590 nm *versus* various concentrations of PSA in PBST solutions. (C) The linear range of (B). The PBST-only sample was set as the blank. $\Delta F_{max} = F - F_0$ was used to measure the variations of the fluorescence intensity, where F is the emission fluorescence intensity at 590 nm and F_0 is the background fluorescence. Error bars show standard deviations ($n = 3$).
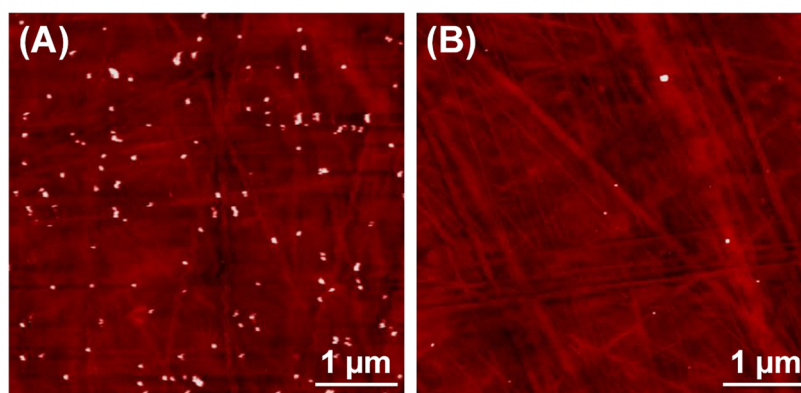

Figure 4. AFM images of PS substrates after Ab2—RBITC—AuNPs were pulled down onto the PSA-immobilized surfaces where the concentration of the pretreated PSA was 1 ng/mL (A) and that pretreated with PBST-only sample (B).

the detection performance of this assay for PSA in serum samples. We first used the horseradish peroxidase (HRP)-based commercial PSA kit to measure the PSA contents in five patients suffering from prostate cancer. Their PSA levels were calculated with the assistance of a standard curve to be 34.3, 21.2, 8.6, 13.4, and 5.3 ng/mL, respectively (Figure S9 in the Supporting Information). Since the clinical detection limit for PSA is 0.1 ng/mL,[5] which is higher than the PSA contents in most patients especially in their earlier stages or after radical prostatectomy, detection of

PSA in patient serum at very low levels is highly associated with improved therapeutic outcomes. To demonstrate this, we diluted the five serum samples 10, 100, 1000, 10^4, and 10^5 times using PBST. The resulting solutions were measured by the commercial ELISA and our activatable probe. As shown in Figure 5, the PSA contents can be detectable by the commercial immunoassay only after 10-fold dilution, where the concentrations of PSA are in the ng/mL level. In contrast to the commercial immunoassay, the novel activatable probe offered much higher sensitivity to
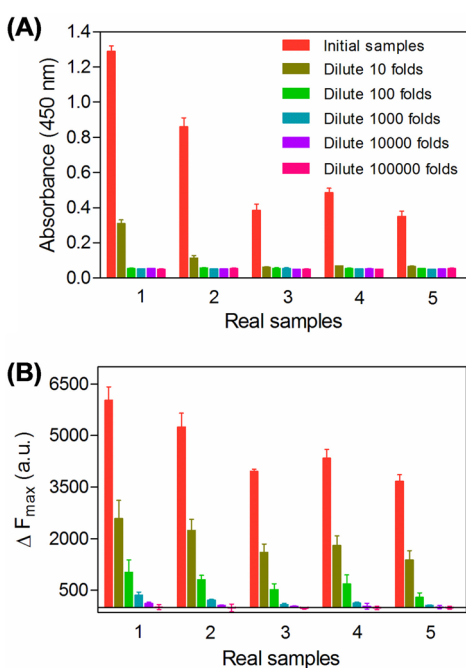
Figure 5. Detection results of the commercially available HRP-based immunoassay (A) and the newly developed fluorescence -activatable immunoassay (B) for PSA in patient serum samples where the contents of PSA were serially diluted by 10-fold. Error bars show standard deviations ($n = 3$).

biomarker detection and thus can detect the PSA contents even when they were diluted 10 000-fold.

This value, at the pg/mL level, is much lower than the detection limit of the commercial immunoassay, demonstrating the potential applications of the newly developed activatable probe in the clinic.

CONCLUSIONS

In this study, we have introduced a new activatable fluorescence probe to allow detection of PSA in patient serum at the pg/mL level. The LOD of this activatable probe is several orders of magnitude lower than the conventional fluorescent immunoassays as well as the current HRP-based immunoassays. The ultrahigh sensitivity of this probe is based on the high loading efficiency of RBITC onto AuNP surfaces and high fluorescence "off–on" properties of RBITC–AuNP pairs. Such improved detection systems would enable the screening of biomarkers at their early stages or after radical prostatectomy, thus providing improved therapeutic outcomes. Although PSA was taken only as an example to demonstrate the proof-of-concept, we expect that this platform can be extended to the detection of other biomarkers clinically required. Lastly, the detection was performed in 96-well PS plates, the most popular detection format in clinical laboratories, especially in developing countries, making this method low-cost and easily adaptable into currently available diagnostic platforms.

MATERIALS AND METHODS

Materials and Instrumentation. Gold nanoparticles with diameters of 15, 30, 60, and 80 nm were purchased from Ted Pella. Rhodamine B isothiocyanate dye, Tween 20, prostate-specific antigen, and bovine serum albumin were purchased from Sigma-Aldrich and were used as received. Phosphate-buffered saline ($10\times$, pH 7.4) was purchased from Mediatech, Inc. and was diluted 10-fold when used. Monoclonal primary anti-human PSA antibody (Ab1, clone no. CHYH1) and secondary anti-human PSA antibody (Ab2, clone no. CHYH2) were purchased from Anogen/Yes Biotech Laboratory, Ltd. PSA-positive serum samples were purchased from Capital Biosciences. PSA (human) ELISA kit was purchased from Abnova Corporation. The 96-well PS plate was purchased from R&D Systems. Deionized water (Millipore Milli-Q grade) with a resistivity of 18.2 MΩ-cm was used throughout this study. The UV–vis spectra of gold colloidal solutions and RBITC solutions were recorded with a Genesys 10s UV–vis spectrophotometer. The fluorescence spectra were collected using an F-7000 fluorescence spectrophotometer (Hitachi, Tokyo, Japan) operating at an excitation wavelength at 530 nm; excitation and emission slit widths were 5 and 5 nm, respectively. The fluorescence intensities in the 96-well plates were collected at 590 nm by a Synergy 2 Multi-Mode microplate reader (Bio-Tek Instruments, Inc.). Dynamic light scattering (DLS) and zeta potential (ζ) were performed on a Zeta Sizer Nano ZS (Malvern Zetasizer 3000HS and He/Ne laser at 632.8 nm at scattering angles of 90° at 25 °C. The fluorescence activation of RBITC was monitored using a Maestro all-optical imaging system (Caliper Life Sciences, Hopkinton, MA, USA). PeakForce QNM mode AFM studies were performed on a Bioscope Catalyst AFM (Bruker, CA, USA) sitting on an inverted microscope (IX71, Olympus, Japan) with a Nanoscope V controller (Bruker, CA, USA) to image the sensor surfaces under

fluid, using a DNP-type cantilever and following routine optimizations for biological AFM.

Preparation of Ab2–RBITC–AuNPs. The procedure of preparing Ab2–RBITC–AuNPs was amenable to all four sized AuNPs depicted in Figure S1. We herein only take 15 nm AuNPs as an example. First, the original citrate-covered AuNPs solution (1 mL) was adjusted by K_2CO_3 (100 mM) to be around pH 9. Then, a stock solution of RBITC (10 mM, 1 μL) was added into the citrate-AuNPs solution with vigorous shaking to allow adsorption of RBITC onto the AuNP surfaces. The resulting mixture was shaken at 600 rpm in the dark for 1 h for sufficient equilibration. After centrifugation (14 000 rpm, 15 min) for three runs, the excess RBITC was removed, and the RBITC-modified AuNP (RBITC–AuNP) pellet was dissolved in pH 9 K_2CO_3 (1 mL, 2 mM) solution. Then, 12 μL of the detection antibody (Ab2, 1 mg/mL) solution was added into the as-prepared RBITC–AuNPs solution. The mixture was shaken at room temperature for 2 h. Ab2–RBITC–AuNPs conjugates were formed, and an excess amount of free Ab2 was removed by centrifugation (14 000 rpm, 15 min) for two runs. After that, the remaining sites of the RBITC layer on AuNP surfaces were passivated by adding 1 mL of 10% BSA in PBS solution into the as-prepared Ab2–RBITC–AuNPs solution. The resulting mixture was shaken for 30 min and washed with PBST for three runs. The resulting pellet was dispersed in 1 mL of PBST and the solution was stored at 4 °C for further use.

Procedures of the Immunoassays. We carried out the sandwich-type immunoassay as follows. The capture antibody Ab1 (4 μg/mL) was first dissolved in 100 mM pH 9.6 Na_2CO_3–$NaHCO_3$ coating buffer. Aliquots of 50 μL of the Ab1 solution were added into each well of the 96-well PS plate. The plate was maintained at 4 °C overnight or at room temperature for 4 h. After that, the solutions were discarded and 200 μL of PBST buffer was added into each well and washed for three runs to remove the unbound capture antibodies. Nonspecific binding sites were blocked by placing

200 μL of 1% BSA in PBS into each well for 1 h at 37 °C, followed by copious rinsing with PBST solutions for three runs. After passivation, to the Ab1-modified wells were added PBST solutions containing varying concentrations of PSA ranging from 0.1 pg/mL to 100 ng/mL. The PBST-only solution was set as the blank. The plate was kept at 37 °C for 1 h and washed with PBST for three runs. Later, 50 μL of Ab2−RBITC−AuNPs solutions was added into the wells and incubated at 37 °C for another 1 h. Ab2−RBITC−AuNPs were pulled down onto the substrate owing to antigen−antibody binding. The unbound Ab2−RBITC−AuNPs were washed away by PBST solutions for four runs and rinsed with deionized water for two runs. Finally, to the wells were added release reagents (1 mM of cysteamine is the optimized solution), and the plate was shaken at 600 rpm for 1 min in the dark. The fluorescence intensities were recorded by a Synergy 2 Multi-Mode microplate reader.

Preparation of RBITC-Conjugated Ab2. RBITC contains an ITC (−N=C=S) group, which is a reactive group commonly used to conjugate with the primary amines of proteins without generating byproducts. First, Ab2 (100 μg) was dissolved in pH 9 K_2CO_3 (2 mM, 1 mL) solution, where the target amine groups in Ab2 were mainly unprotonated. One milligram of RBITC was dissolved in 1 mL of anhydrous dimethyl sulfoxide (DMSO). A 3.6 μL amount of freshly prepared RBITC solution was added into the as-prepared Ab2 solution to give a reaction ratio of 10 RBITC per each Ab2. The reaction was performed in a tube that was wrapped with foil. The mixture was shaken at room temperature for 1 h. The unreacted RBITC was removed by dialysis. The products were measured by fluorescence spectroscopy (Figure S8). The fluorescence peak at around 580 nm demonstrated that RBITC had been successfully labeled onto Ab2. In general, only several RBITC molecules are conjugated to each antibody because higher conjugations may cause internal quenching between the dyes and influence the immunogenic activity of Ab2.

Conflict of Interest: The authors declare no competing financial interest.

Supporting Information Available: Details of characterizing gold nanoparticles and various conjugates described here can be found in the Supporting Information. This material is available free of charge *via* the Internet at http://pubs.acs.org.

REFERENCES AND NOTES

1. Rifai, N.; Gillette, M. A.; Carr, S. A. Protein Biomarker Discovery and Validation: The Long and Uncertain Path to Clinical Utility. *Nat. Biotechnol.* **2006**, *24*, 971–983.
2. Swierczewska, M.; Liu, G.; Lee, S.; Chen, X. High-Sensitivity Nanosensors for Biomarker Detection. *Chem. Soc. Rev.* **2012**, *41*, 2641–2655.
3. Hanash, S. M.; Baik, C. S.; Kallioniemi, O. Emerging Molecular Biomarkers—Blood-Based Strategies to Detect and Monitor Cancer. *Nat. Rev. Clin. Oncol.* **2011**, *8*, 142–150.
4. Nagrath, S.; Sequist, L. V.; Maheswaran, S.; Bell, D. W.; Irimia, D.; Ulkus, L.; Smith, M. R.; Kwak, E. L.; Digumarthy, S.; Muzikansky, A.; *et al*. Isolation of Rare Circulating Tumour Cells in Cancer Patients by Microchip Technology. *Nature* **2007**, *450*, 1235–1239.
5. Giljohann, D. A.; Mirkin, C. A. Drivers of Biodiagnostic Development. *Nature* **2009**, *462*, 461–464.
6. Perfézou, M.; Turner, A.; Merkoçi, A. Cancer Detection Using Nanoparticle-Based Sensors. *Chem. Soc. Rev.* **2012**, *41*, 2606–2622.
7. Kwong, G. A.; von Maltzahn, G.; Murugappan, G.; Abudayyeh, O.; Mo, S.; Papayannopoulos, I. A.; Sverdlov, D. Y.; Liu, S. B.; Warren, A. D.; Popov, Y.; *et al*. Mass-Encoded Synthetic Biomarkers for Multiplexed Urinary Monitoring of Disease. *Nat. Biotechnol.* **2013**, *31*, 63–70.
8. Hu, M.; Yan, J.; He, Y.; Lu, H.; Weng, L.; Song, S.; Fan, C.; Wang, L. Ultrasensitive, Multiplexed Detection of Cancer Biomarkers Directly in Serum by Using a Quantum Dot-Based Microfluidic Protein Chip. *ACS Nano* **2010**, *4*, 488–494.
9. Huang, C. S.; George, S.; Lu, M.; Chaudhery, V.; Tan, R.; Zangar, R. C.; Cunningham, B. T. Application of Photonic Crystal Enhanced Fluorescence to Cancer Biomarker Microarrays. *Anal. Chem.* **2011**, *83*, 1425–1430.
10. Dubertret, B.; Calame, M.; Libchaber, A. J. Single-Mismatch Detection Using Gold-Quenched Fluorescent Oligonucleotides. *Nat. Biotechnol.* **2001**, *19*, 365–370.
11. Maxwell, D. J.; Taylor, J. R.; Nie, S. Self-Assembled Nanoparticle Probes for Recognition and Detection of Biomolecules. *J. Am. Chem. Soc.* **2002**, *124*, 9606–9612.
12. Oh, E.; Hong, M. Y.; Lee, D.; Nam, S. H.; Yoon, H. C.; Kim, H. S. Inhibition Assay of Biomolecules Based on Fluorescence Resonance Energy Transfer (FRET) between Quantum Dots and Gold Nanoparticles. *J. Am. Chem. Soc.* **2005**, *127*, 3270–3271.
13. Mayilo, S.; Ehlers, B.; Wunderlich, M.; Klar, T. A.; Josel, H. P.; Heindl, D.; Nichtl, A.; Kürzinger, K.; Feldmann, J. Competitive Homogeneous Digoxigenin Immunoassay Based on Fluorescence Quenching by Gold Nanoparticles. *Anal. Chim. Acta* **2009**, *646*, 119–122.
14. Nam, J. M.; Thaxton, C. S.; Mirkin, C. A. Nanoparticle-Based Bio-Bar Codes for the Ultrasensitive Detection of Proteins. *Science* **2003**, *301*, 1884–1886.
15. Thaxton, C. S.; Elghanian, R.; Thomas, A. D.; Stoeva, S. I.; Lee, J. S.; Smith, N. D.; Schaeffer, A. J.; Klocker, H.; Horninger, W.; Bartsch, G.; *et al*. Nanoparticle-Based Bio-Barcode Assay Redefines "Undetectable" PSA and Biochemical Recurrence after Radical Prostatectomy. *Proc. Natl. Acad. Sci. U.S.A.* **2009**, *106*, 18437–18442.
16. Chen, Z.; Tabakman, S. M.; Goodwin, A. P.; Kattah, M. G.; Daranciang, D.; Wang, X.; Zhang, G.; Li, X.; Liu, Z.; Utz, P. J.; *et al*. Protein Microarrays with Carbon Nanotubes as Multicolor Raman Labels. *Nat. Biotechnol.* **2008**, *26*, 1285–1292.
17. Rodríguez-Lorenzo, L.; de la Rica, R.; Alvarez-Puebla, R. A.; Liz-Marzán, L. M.; Stevens, M. M. Plasmonic Nanosensors with Inverse Sensitivity by Means of Enzyme-Guided Crystal Growth. *Nat. Mater.* **2012**, *11*, 604–607.
18. De la Rica, R.; Stevens, M. M. Plasmonic ELISA for the Ultrasensitive Detection of Disease Biomarkers with the Naked Eye. *Nat. Nanotechnol.* **2012**, *7*, 821–824.
19. Tabakman, S. M.; Lau, L.; Robinson, J. T.; Price, J.; Sherlock, S. P.; Wang, H.; Zhang, B.; Chen, Z.; Tangsombatvisit, S.; Jarrell, J. A.; *et al*. Plasmonic Substrates for Multiplexed Protein Microarrays with Femtomolar Sensitivity and Broad Dynamic Range. *Nat. Commun.* **2011**, *2*, 466.
20. Park, J. S.; Cho, M. K.; Lee, E. J.; Ahn, K. Y.; Lee, K. E.; Jung, J. H.; Cho, Y.; Han, S. S.; Kim, Y. K.; Lee, J. A Highly Sensitive and Selective Diagnostic Assay Based on Virus Nanoparticles. *Nat. Nanotechnol.* **2009**, *4*, 259–264.
21. Swierczewska, M.; Lee, S.; Chen, X. The Design and Application of Fluorophore−Gold Nanoparticle Activatable Probes. *Phys. Chem. Chem. Phys.* **2011**, *13*, 9929–9941.
22. Dulkeith, E.; Ringler, M.; Klar, T. A.; Feldmann, J.; Javier, A. M.; Parak, W. J. Gold Nanoparticles Quench Fluorescence by Phase Induced Radiative Rate Suppression. *Nano Lett.* **2005**, *5*, 585–589.
23. Liu, D.; Wang, S.; Swierczewska, M.; Huang, X.; Bhirde, A. A.; Sun, J.; Wang, Z.; Yang, M.; Jiang, X.; Chen, X. Highly Robust, Recyclable Displacement Assay for Mercuric Ions in Aqueous Solutions and Living Cells. *ACS Nano* **2012**, *6*, 10999–11008.
24. Ghosh, D.; Girigoswami, A.; Chattopadhyay, N. Superquenching of Coumarin 153 by Gold Nanoparticles. *J. Photochem. Photobiol. A−Chem.* **2012**, *242*, 44–50.
25. Griffin, J.; Singh, A. K.; Senapati, D.; Rhodes, P.; Mitchell, K.; Robinson, B.; Yu, E.; Ray, P. C. Size- and Distance-Dependent Nanoparticle Surface-Energy Transfer (NSET) Method for Selective Sensing of Hepatitis C Virus RNA. *Chem.—Eur. J.* **2009**, *15*, 342–351.
26. Fan, C.; Wang, S.; Hong, J.; Bazan, G. C.; Plaxco, K. W.; Heeger, A. J. Beyond Superquenching: Hyper-Efficient Energy

Transfer from Conjugated Polymers to Gold Nanoparticles. *Proc. Natl. Acad. Sci. U.S.A.* **2003**, *100*, 6297–6301.

27. Stadler, A. L.; Delos Santos, J. O.; Stensrud, E. S.; Dembska, A.; Silva, G. L.; Liu, S.; Shank, N. I.; Kunttas-Tatli, E.; Sobers, C. J.; Gramlich, P. M. E.; *et al*. Fluorescent DNA Nanotags Featuring Covalently Attached Intercalating Dyes: Synthesis, Antibody Conjugation, and Intracellular Imaging. *Bioconjugate Chem.* **2011**, *22*, 1491–1502.

28. Rissin, D. M.; Kan, C. W.; Campbell, T. G.; Howes, S. C.; Fournier, D. R.; Song, L.; Piech, T.; Patel, P. P.; Chang, L.; Rivnak, A. J.; *et al*. Single-Molecule Enzyme-Linked Immu-nosorbent Assay Detects Serum Proteins at Subfemtomolar Concentrations. *Nat. Biotechnol.* **2010**, *28*, 595–599.

29. Kumar, A. S.; Ye, T.; Takami, T.; Yu, B. C.; Flatt, A. K.; Tour, J. M.; Weiss, P. S. Reversible Photo-Switching of Single Azobenzene Molecules in Controlled Nanoscale Environments. *Nano Lett.* **2008**, *8*, 1644–1648.

30. Liu, D.; Xie, Y.; Shao, H.; Jiang, X. Using Azobenzene-Embedded Self-Assembled Monolayers to Photochemically Control Cell Adhesion Reversibly. *Angew. Chem., Int. Ed.* **2009**, *48*, 4406–4408.

31. Liu, D.; Chen, W.; Sun, K.; Deng, K.; Zhang, W.; Wang, Z.; Jiang, X. Resettable, Multi-Readout Logic Gates Based on Controllably Reversible Aggregation of Gold Nanoparticles. *Angew. Chem., Int. Ed.* **2011**, *50*, 4103–4107.

32. De, M.; Rana, S.; Akpinar, H.; Miranda, O. R.; Arvizo, R. R.; Bunz, U. H. F.; Rotello, V. M. Sensing of Proteins in Human Serum Using Conjugates of Nanoparticles and Green Fluorescent Protein. *Nat. Chem.* **2009**, *1*, 461–465.